PHYSICAL REVIEW D **85,** 094006 (2012)

Systematics of radial and angular-momentum Regge trajectories of light nonstrange $q\bar{q}$-states

Pere Masjuan,[1,*] Enrique Ruiz Arriola,[2,†] and Wojciech Broniowski[3,4,‡]

[1]*Departamento de Física Teórica y del Cosmos and CAFPE, Universidad de Granada, E-18071 Granada, Spain*
[2]*Departamento de Física Atómica, Molecular y Nuclear and Instituto Carlos I de Física Teórica y Computacional, Universidad de Granada, E-18071 Granada, Spain*
[3]*The H. Niewodniczański Institute of Nuclear Physics, PL-31342 Kraków, Poland*
[4]*Institute of Physics, Jan Kochanowski University, PL-25406 Kielce, Poland*

(Received 22 March 2012; published 7 May 2012)

We reanalyze the radial (n) and angular-momentum (J) Regge trajectories for all light-quark states with baryon number zero listed in the 2011 edition of the Particle Data tables. The parameters of the trajectories are obtained with linear regression, with weight of each resonance inversely proportional to its half-width squared, $(\Gamma/2)2$. That way, we are side-stepping possible channel-dependent and model-dependent extractions of the resonance parameters and are able to undertake an error analysis. The method complies to the fact that the pole position of the resonance is typically shifted from channel-dependent extractions by $\sim\Gamma/2$. This is also a feature of the large-N_c limit of QCD, where the masses change by $\Gamma/2$ when evolving from $N_c = 3$ to $N_c = \infty$. Our value for the slope of the radial Regge trajectories is $a = 1.35(4)$ GeV^2. We discuss the fundamental issue whether the masses of the light-quark nonstrange states fit into a universal pattern $M_{nJ}^2 = a(n + J) + b$, as suggested by Afonin, and also predicted by some holographic models. Our joint linear-regression analysis in the (n, J, M^2) Regge planes indicates, at a statistically significant level of 4.5 standard deviations, that the slopes of the radial Regge trajectories are larger from the angular-momentum slopes. Thus, no strict universality of slopes occurs in the light nonstrange meson spectra.

DOI: 10.1103/PhysRevD.85.094006 PACS numbers: 14.40.−n, 12.38.−t, 12.39.Mk

I. INTRODUCTION

The study of regularities in the hadronic spectrum has been a recurrent subject in the quark model [1], as it allows not only to check our current understanding of strong interactions, but also to predict possible missing states. In the case of light-quark mesons, which is the subject of the present study, the quark-hadron duality [2] implies QCD constraints based on the operator product expansion of a two-point correlation function with some given mesonic quantum numbers (say J). In particular,

$$f_{nJ}^2/(dM_{nJ}^2/dn) \to \text{const}, \tag{1}$$

where M_{nJ} is the nth mass of the meson and f_{nJ} the corresponding vacuum decay amplitude. More than a decade ago, Anisovich, Anisovich, and Sarantsev [3] suggested that mesons could be grouped into *radial* Regge trajectories of the form

$$M_n^2 = M_0^2 + n\mu^2, \tag{2}$$

where M_0 is the mass of the lowest-lying meson on each corresponding trajectory and μ^2 is the slope parameter. According to Ref. [3], the slope is approximately the same for *all* the trajectories considered: $\mu^2 = 1.25(15)$ GeV^2. The uncertainly was estimated based on the spread of the different results for each meson family. In addition, some missing states predicted from Eq. (2) have indeed been confirmed and included in the latest edition of the Particle Data Group (PDG) tables [4]. Furthermore, Ref. [3] also analyzed the venerable angular-momentum Regge trajectories [5] (for a review see, e.g., [6]), which motivated the original (rubber) string models [7] (for a review see, e.g., [8,9]). Similar results were found in Ref. [10]. Moreover, the large degeneracy [11] of the daughter Regge trajectories is capable of producing the Hagedorn growth of the hadronic spectra [11,12] (see Refs. [13,14] for a recent reanalysis).

In a remarkable paper, Afonin [15] (see also [16]) analyzed jointly the radial and angular-momentum trajectories and argued that they merge into a single pattern

$$M^2(n, J) = a(n + J) + c, \tag{3}$$

unveiling a kind of hydrogenlike accidental degeneracy, with a harmonic oscillator mass-squared spectrum. All these phenomenological findings provide some confidence on the string picture of hadrons, where the square of the mass is the fundamental dynamical quantity. Together with the QCD short-distance constraint of Eq. (1), we may then infer that mesonic vacuum decay amplitudes tend to a constant in the upper part of the spectrum.

Regardless of the success of the radial Regge trajectories, it is important to note that the resonance parameters, such as mass, width, or coupling constants, depend on the

*masjuan@ugr.es
†earriola@ugr.es
‡Wojciech.Broniowski@ifj.edu.pl

definitions and are sensitive to the background, i.e., to the particular process used to extract the resonance from the experimental data. This poses the relevant question of what the precise meaning of Eq. (2) is, and, moreover, in what sense is QCD compatible with such an analysis. In the present work, we reanalyze this problem, carrying out global linear-regression fits with the uncertainty of the resonance position proportional to its width, Γ. Specifically, we use weights inversely proportional to the square of the resonance half-width. The approach is consistent with the fact that the pole position of the resonance is typically shifted from channel-dependent extractions by about $\Gamma/2$. Also, within the large-N_c QCD [17,18] (see, e.g., [19] for a review), where the strong coupling constant is assumed to scale as $g \sim 1/\sqrt{N_c}$, the meson masses change by $\Gamma/2$ when evolved from $N_c = 3$ to $N_c = \infty$, as has been exploited intensely in Refs. [20–27].

We note that within the AdS/CFT proposal (for a review see, e.g., [28]) there have been attempts to formulate holographic models (the so-called soft-wall models) with linear confinement [29] and, likewise, their light-cone relatives [30], complying to the ansatz of Eq. (2). We recall that all these AdS/CFT-inspired models are claimed to operate for large t'Hooft couplings, i.e., $g \sim 1/N_c$.

As we will elaborate in detail, our main finding, after considering the resonance width uncertainties, is to confirm the result of Ref. [3] with the updated data, as we find $\mu^2 = 1.35(4)$ GeV^2. On the other hand, our analysis in the (n, J, M^2) Regge planes shows that at a statistically significant level of 4.5 standard deviations the slopes of the radial Regge trajectories are larger from the slopes of the angular-momentum trajectories. Therefore, no strict universality of slopes occurs in the light nonstrange meson sector.

The plan of the paper is as follows. In Sec. II, we motivate our choice for the weight in the linear-regression analysis.

In Sec. III, we discuss in detail, through the use of the present PDG tables, how the different states are grouped into the radial Regge trajectories. Whenever possible, we try to keep the successful choice of Ref. [3] taking into account the assumed uncertainties. In Sec. III H on, we enlarge the choice of Ref. [3] to complete all the light unflavored states collected in the PDG. The update of the angular-momentum Regge trajectories is considered in Sec. IV. In Sec. V, we discuss, as originally suggested by Afonin, simultaneously the radial and angular-momentum trajectories. Finally, in Sec. VI we summarize our results and draw our main conclusions.

Throughout this work, we use the up-to-date edition of the PDG tables [4]. The symbol q stand for the light quarks, u or d.

II. UNCERTAINTIES OF RESONANCE POSITIONS

As already mentioned in the Introduction, in order to properly size the meaning of the radial Regge trajectories for resonant states it is important to review the well-known features of the quantum-mechanical decay process relevant to our discussion. The rigorous quantum-mechanical definition of a resonance with given quantum numbers corresponds to a pole in the second Riemann sheet in the (analytically continued) partial-wave amplitude of the considered scattering channel [31]. This definition becomes independent on the background, whereas the corresponding residue provides the amplitude to produce that resonance in the given process.

However, although quoting the complex pole and the complex residue would be superior and highly desirable, for practical reasons this is not what one typically finds in the PDG tables [4], with very few exceptions. As a matter of fact, several definitions besides the pole in the second Riemann sheet are employed, such as a pole in the K-matrix, the Breit-Wigner resonance, the location of a maximum in the speed plot, time delay, etc. (see, e.g., [32,33]).

A resonance may be interpreted as a superposition of states with a given mass distribution on the real axis, approximately spanning the $M \pm \Gamma/2$ interval. Of course, the shape of the distribution depends on the particular process in which the resonance is produced, and thus on the background. Clearly, while all the definitions converge for narrow resonances, even for broad states we expect the masses obtained from various methods to be compatible within their corresponding $M \pm \Gamma/2$ intervals. As stated above, the values listed by the PDG for a given resonance correspond to different choices of the definition and/or production processes, but mostly the results are compatible within the estimated width differences. This clearly provides an upper bound on the uncertainty of the resonance position for different resonance parameter definitions. For shortness, we refer to this mass uncertainty estimate of the resonance mass as the *half-width rule*.[1]

Quite remarkably, there is a QCD scenario where the half-width rule estimate becomes parametrically small for *all* the resonances in the mesonic spectrum. In the large-N_c limit of QCD [17,18] (see, e.g., [19] for a review using effective Lagrangians) mesons become stable, i.e., their masses are $M = \mathcal{O}(N_c^0)$, while their widths are suppressed, $\Gamma = \mathcal{O}(1/N_c)$, such that the ratio $\Gamma/M = \mathcal{O}(1/N_c)$. This expectation of the large-N_c limit seems to be fulfilled very well in the real $N_c = 3$ world, since one finds for the light-quark mesons an average value $\Gamma/M = 0.12(8)$ (to be compared with a rule of thumb $1/N_c = 0.33$ for $N_c = 3$) [34]. This feature is visualized in Fig. 1. Of course, there are exceptions to this average ratio, but they are scarce within the given confidence interval. In fact, only just one state ($\sigma = f_0(600)$) goes over the 1/3-value [34].

[1]Of course, the width itself has an uncertainty which may eventually enlarge the global indetermination in the resonance mass.

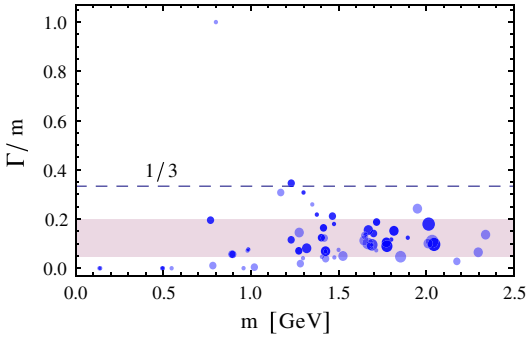

FIG. 1 (color online). The ratio of width to mass for the light-quark meson states. The surface of each point is proportional to the $(2J+1)$ spin degeneracy, while the intensity is proportional to the isospin degeneracy $(2I+1)$. The band corresponds to the average $\pm$ standard deviation bounds, $\Gamma/M = 0.12(8)$.

A complementary way of connecting parametrically the mass shift and the decay width is as follows. One starts with the leading-N_c resonance Lagrangian [19], recalling that the three and higher n-mesonic interactions are $\mathcal{O}(N_c^{1-n/2})$ [17,18]. Thus, the mass shift is computed as a loop integral via the self-energy whose imaginary part corresponds to the decay width of the particles inside the loop according to the Cutkosky rules. This argument makes it clear that the $1/N_c$ scaling of the mass shift and the width are exactly the same and bound by $\mathcal{O}(1/N_c)$, although the numerical values of the two quantities may not coincide exactly. The point of this discussion is that if we take the leading-$1/N_c$ resonance mass, its *systematic* uncertainty is parametrically indistinguishable from the decay width, since they are the real and imaginary parts of the self-energy, respectively. As pointed out in Ref. [35], the role of the mass shift is crucial when determining the properties of two-point correlator functions.

Within this framework, the half-width rule has been used recently [34,36] for the case of the scalar and pseudoscalar mesons with rather interesting results regarding the identification of glueball states and chiral symmetry doublets. Here, we extend these ideas to the rest of the light-quark meson spectrum. Specifically, to incorporate the half-width rule in practice, we take[2]

$$\chi^2 = \sum_n \left(\frac{M_n^2 - M_{n,\mathrm{exp}}^2}{\Gamma_n M_n} \right)^2, \tag{4}$$

for the linear-regression fit, where the radial Regge formula, Eq. (2), is used as the model. Note that in doing so, we are just saying that Eq. (2) is fulfilled within the uncertainty $M_n^2 = \mu^2 n + M_0^2 \pm \Gamma_n M_n$. Moreover, we will stay within the linear ansatz as the half-width rule yields insensitivity to small nonlinearities as analyzed, e.g., in Ref. [37] for n-trajectories or in Ref. [38] for J-trajectories.

[2]There is an alternative fit with $\chi^2 = \sum_n (\frac{M_n - M_{n,\mathrm{exp}}}{\Gamma_n/2})2$ which does not alter much in the results. Actually, both χ^2 functions are particular examples of the more general maximum-likelihood method, where the resonance production profile is assumed to be Gaussian. For a discussion on other profiles, in particular, for the ubiquitous Breit-Wigner shape, see the Appendix for details.

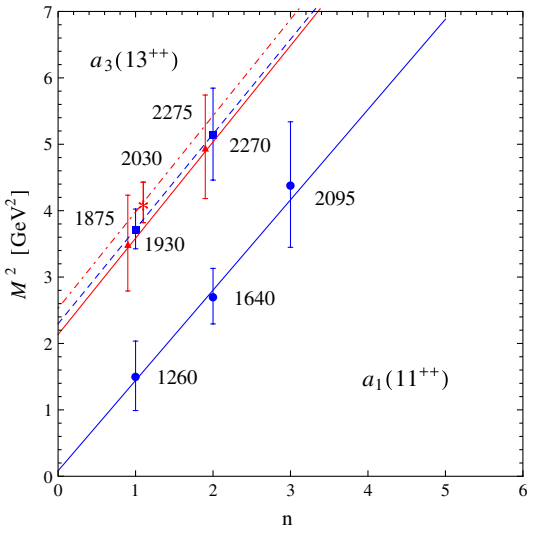

FIG. 2 (color online). The (n, M^2) plots for the states $a_1(1^{++})$ (lower solid and dashed lines) and $a_1(3^{++})$ (upper solid and dash-dotted lines). Error bars correspond to taking $\Delta M^2 = \pm \Gamma M$.

III. RADIAL REGGE TRAJECTORIES

The construction of a meson Regge trajectory requires a choice on the possible meson assignments. The analysis of the radial Regge trajectories we are carrying out consists of two stages: The first one reanalyzes the results of Ref. [3] with the inclusion of more states from the updated PDG tables [4], while from Sec. III H on we deal with meson families not considered in Ref. [3]. To facilitate the comparison, we follow as close as possible the presentation of Ref. [3].

We motivate our selections with rather detailed discussions. The reader interested in the results only may jump to Sec. III N.

In all our M^2-plots we take, in line with the half-width rule, the error to be given by $\Delta M^2 = \pm \Gamma M$.

A. $a_1(11^{++})$ and $a_3(13^{++})$

Compared to Ref. [3], we consider four different trajectories: two for the $a_1(11^{++})$ states (lower solid and dashed lines in Fig. 2) and two for the $a_3(13^{++})$ states (upper solid and dash-dotted lines in Fig. 2). The first trajectory for the $a_1(11^{++})$ states contains $a_1(1260)$, $a_1(1640)$, and $a_1(2095)$. The $a_1(2340)$ state (now called $a_1(2270)$), assumed in Ref. [3] to belong to this trajectory, is now used in the daughter trajectory for the $a_1(11^{++})$, together with a new state not considered in Ref. [3], the $a_1(1930)$. The linear fit to the first trajectory for the $a_1(11^{++})$ states yields

$\mu^2 = 1.36(49)$ GeV^2 with χ^2 per degrees of freedom, $\chi^2/\mathrm{DOF} = 0.12$ (lower solid line in Fig. 2). For the second trajectory $\mu^2 = 1.43(73)$ GeV^2 (dashed line on Fig. 2). This trajectory has only two states and it will not be considered for the final compilation.

In the case of the $a_3(13^{++})$ trajectories, the first one contains the new $a_3(1875)$ state together with the $a_3(2275)$, yielding $\mu^2 = 1.5(1.1)$ GeV^2 (upper solid line in Fig. 2) and the second trajectory contains only the $a_3(2030)$ state [dash-dotted line parallel to the $a_3(13^{++})$ trajectory].

B. $\eta(00^{-+})$ and $\eta_2(02^{-+})$

Figure 3 shows the $\eta(00^{-+})$ and $\eta_2(02^{-+})$ states where, due to two independent flavor components $q\bar{q}$ and $s\bar{s}$, both yield two trajectories. The $\eta(00^{-+})q\bar{q}$ contains five states: $\eta(548)$, $\eta(1295)$, $\eta(1760)$, $\eta(2100)$, and $\eta(2320)$ (lower solid line in Fig. 3), where the first state, $\eta(548)$, is not used in the linear fit. In Ref. [3], the state $\eta(2100)$ was predicted, while nothing was said about the $\eta(2320)$. Both states, now listed by the PDG, are incorporated in our study. The fit yields $\mu^2 = 1.33(11)$ GeV^2 with $\chi^2/\mathrm{DOF} = 0.26$.

The $\eta(00^{-+})s\bar{s}$ trajectory with four states: $\eta(958)$, $\eta(1475)$, $\eta(2010)$, and $\eta(2225)$, yields $\mu^2 = 1.36(14)$ GeV^2 with $\chi^2/\mathrm{DOF} = 0.44$. The $\eta(2010)$ was predicted in Ref. [3] under the name $\eta(1900)$ and now is listed in the PDG tables.

In Ref. [3], only one state with mass near 1440 MeV was considered. Now, it is well established that in this energy region there are two different η states, the $\eta(1405)$ and the $\eta(1475)$. The first one, however, is not unambiguously located and it is considered to be a glueball (see the mini-review about this state on the PDG tables), therefore we exclude it from our fitting procedure. The second state is included in the $s\bar{s}$ trajectory.

The $\eta(02^{-+})q\bar{q}$ trajectory yields $\mu^2 = 1.32(32)$ GeV^2, with $\chi^2/\mathrm{DOF} = 0.22$. This trajectory contains $\eta_2(1645)$, $\eta_2(2030)$, and $\eta_2(2250)$. The $\eta(02^{-+})s\bar{s}$ trajectory, which contains only one $\eta_2(1870)$ state, is drawn parallel to the nonstrange case.

C. $\rho_1(11^{--})$ and $\rho_3(13^{--})$

The two trajectories for $\rho_1(11^{--})$ are depicted in Fig. 4. The first one contains $\rho(770)$, $\rho(1450)$, $\rho(1900)$, and $\rho(2150)$. As explained by the PDG, it is not clear what values for the mass and width one should use for $\rho(1900)$. We choose $M = 1.870(30)$ GeV and $\Gamma = 0.150(20)$ GeV. The linear fit (solid line in Fig. 4) yields $\mu^2 = 1.43(13)$ GeV^2 with $\chi^2/\mathrm{DOF} = 0.09$.

The second trajectory contains $\rho(1700)$, $\rho(2000)$, and $\rho(2270)$. These last two states were predicted by Ref. [3] and now are listed in the PDG compilation. The $\rho(1700)$ and $\rho(2000)$ states, however, are controversial and need confirmation. The corresponding slope trajectory is $\mu^2 = 1.08(47)$ GeV^2 with a $\chi^2/\mathrm{DOF} = 0.004$ although it is drawn in Fig. 4 as parallel to the $q\bar{q}$ trajectory due to the lack of confirmation of these states. There is a new state in the PDG tables called $\rho(1570)$, which also needs further confirmation because it might reflect a threshold effect or an Okubo-Zweig-Iizuka-rule-suppressed decay mode of the $\rho(1700)$ (see the mini-review about this issue on PDG). We do not include it on our analysis, either.

In addition to Ref. [3], we have also considered the $\rho_3(13^{--})$ states, which include $\rho_3(1690)$, $\rho_3(1990)$, and $\rho_3(2250)$. The slope for this trajectory is $\mu^2 = 1.19(32)$ GeV^2 with $\chi^2/\mathrm{DOF} = 0.05$. Neither $\rho_3(1690)$

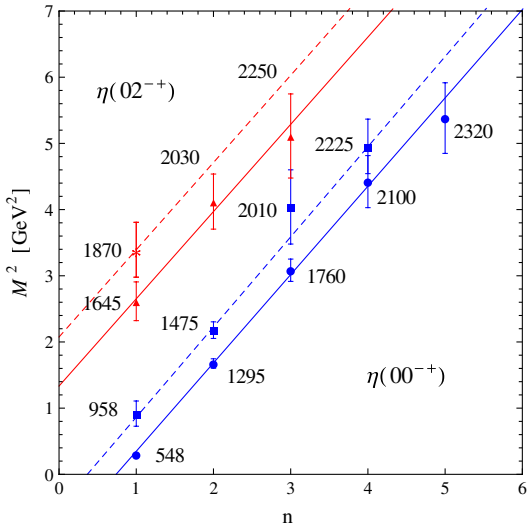

FIG. 3 (color online). The (n, M^2) plots for the $\eta(00^{-+})$ (lower solid and dashed lines) and $\eta_2(02^{-+})$ (upper solid and dashed lines) trajectories. Error bars correspond to taking $\Delta M^2 = \pm\Gamma M$.

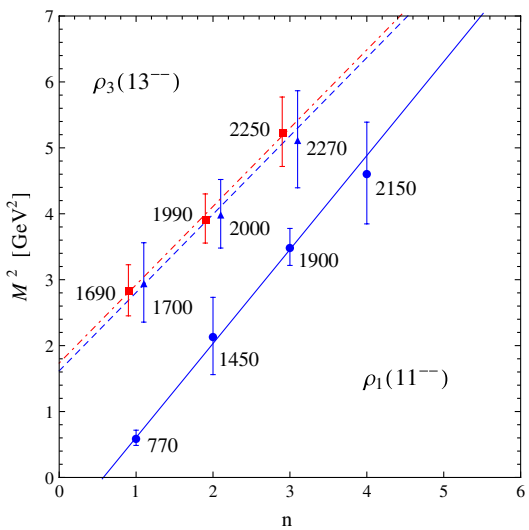

FIG. 4 (color online). The (n, M^2) plots for the states $\rho_1(11^{--})$ (solid and dashed lines, respectively), and the $\rho_3(13^{--})$ states (dash-dotted line). Error bars correspond to taking $\Delta M^2 = \pm\Gamma M$.

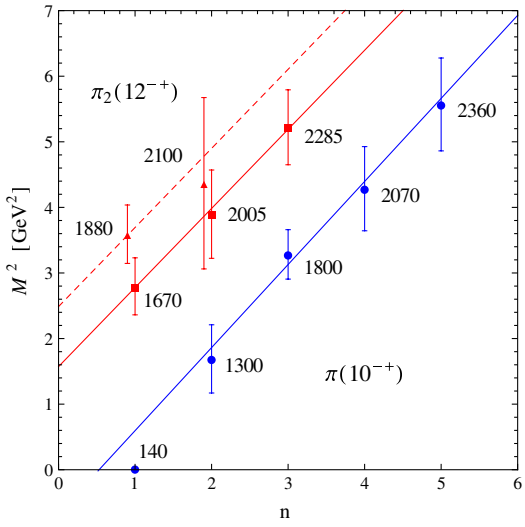

FIG. 5 (color online). The (n, M^2) plots for the $\pi(10^{-+})$ (lower solid line) and $\pi_2(12^{-+})$ (upper solid and dashed lines) trajectories. Error bars correspond to taking $\Delta M^2 = \pm\Gamma M$.

nor $\rho_3(2250)$ are well-established resonances and we just quote them for completeness. We do not use the slope prediction for this trajectory in our later average result.

D. π and π_2

For the $\pi(10^{-+})$ trajectory (lower solid line in Fig. 5), composed of $\pi(1300)$, $\pi(1800)$, $\pi(2070)$, and $\pi(2360)$, the fit produces $\mu^2 = 1.27(27)$ GeV^2 with $\chi^2/\mathrm{DOF} = 0.16$, where the stable $\pi(140)$ state is not used in the fit.[3] We update the trajectory including the $\pi(2070)$ and $\pi(2360)$ states originally predicted in Ref. [3].

The $\pi_2(12^{-+})$ states produce two trajectories. The first one includes $\pi_2(1670)$ and two new states predicted in Ref. [3]: $\pi_2(2005)$ and $\pi_2(2285)$. The fit yields $\mu^2 = 1.21(36)$ GeV^2 with $\chi^2/\mathrm{DOF} = 0.02$ (solid upper line in Fig. 5). The second trajectory has two new states, not predicted in Ref. [3]: $\pi_2(1880)$ and $\pi_2(2100)$. The heaviest π_2, with the mass of 2.090(29) GeV and the width of 0.625 (50) GeV, has still to be confirmed. Conversely, if we use the fitted daughter trajectory with this state omitted, we predict its mass to be around 2.19(13) GeV.

E. $a_0(10^{++})$, $a_2(12^{++})$, and $a_4(14^{++})$

In Ref. [3], the experimental information in the $a_0(10^{++})$, $a_2(12^{++})$, and $a_4(14^{++})$ sector was scarce and could not fix the μ^2 slope uniquely. Therefore, two different slopes, $\mu^2 = 1.38$ GeV^2 and $\mu^2 = 1.1$ GeV^2 were deduced depending on the states included, and in fact $\mu^2 = 1.1$ GeV^2 predicted a yet unobserved new state $a_0(1800)$. Hence, $\mu^2 = 1.38$ GeV^2 is favored currently and we accept the classification of Ref. [3], with the $a_0(10^{++})$, $a_2(12^{++})$, and $a_4(14^{++})$ trajectories and the $a_2(12^{++})$ split into two daughters. The $a_0(10^{++})$ contains $a_0(980)$, $a_0(1450)$,[4] and $a_0(2020)$. The prediction for the slope is $\mu^2 = 1.42(26)$ GeV^2 with $\chi^2/\mathrm{DOF} = 0.48$. The $a_0(2260)$ predicted in Ref. [3] has not been seen yet and in our present description should be located around 2.29 (12) GeV.

Two trajectories for $a_2(12^{++})$ are presented. The lower trajectory contains $a_2(1320)$, $a_2(1700)$, and $a_2(2175)$,[5] giving $\mu^2 = 1.39(26)$ GeV^2 with a $\chi^2/\mathrm{DOF} = 0.24$. The previously predicted $a_2(2400)$ Ref. [3] has not been seen yet. It is also predicted within our trajectory to have $M = 2.42(17)$ GeV.

The upper trajectory contains $a_2(2030)$ and $a_2(2255)$. The $a_2(2030)$ is an average of different experimental determinations (under two different names) from the PDG compilation. In the 1999 PDG edition, a state called $a_2(1990)$ was introduced, while in 2001 this state was updated to become $a_2(2030)$ by Ref. [39], but not modified in the PDG review. Since then, $a_2(2030)$ appears under two different entries in the PDG compilation, hence one of them is redundant. The mass and width for $a_2(2030)$ are not averaged by the PDG, where just the three different measurements are presented. We average them with the result 2021(14) MeV for the mass and 220(23) MeV for the width. This trajectory would produce $\mu^2 = 1.0(7)$ GeV^2.

Another problem to face for the upper a_2 trajectory is the presence of two very close resonances, $a_2(1950)$ with the mass of 1950(50) MeV and the width of 187(50) MeV, and $a_2(2030)$. It is argued in Ref. [39] that it is necessary to obtain a better fit to the data. As a matter of fact, due to the large errors of the mass position and widths, these states might easily be a single state. For the presented reasons, we do not use this trajectory for our average slope value.

Finally, the $a_4(14^{++})$ trajectory contains $a_4(2040)$ and $a_4(2255)$ and the slope turns out to be $\mu^2 = 1.0(8)$ GeV^2. We draw, however, a parallel line to the main (solid) trajectory in Fig. 6.

F. $f_2(02^{++})$

In Ref. [3], it was not possible to discriminate the slopes $\mu^2 = 1.1$ GeV^2 or $\mu^2 = 1.38$ GeV^2 for the $f_2(02^{++})$ sector with the 12 available states in year 2000. The currently listed 18 states favor the second slope.

Figure 2(c) of Ref. [3] shows a quadruplet of trajectories wtih two flavor components, $q\bar{q}$ and $s\bar{s}$. With the inclusion of the additional 6 new states, we find that an overall satisfactory update of Ref. [3] is given by the scheme presented in Fig. 7 (left panel) requiring some reshuffling which we describe below. We name these trajectories, f_2^a,f_2^b, f_2^c, and f_2^d.

[3]One expects a strong nonlinearity for the Goldstone bosons, see, e.g., Ref. [34].

[4]Called before $a_0(1520)$.

[5]Named before $a_2(1660)$ and $a_2(2100)$, respectively.

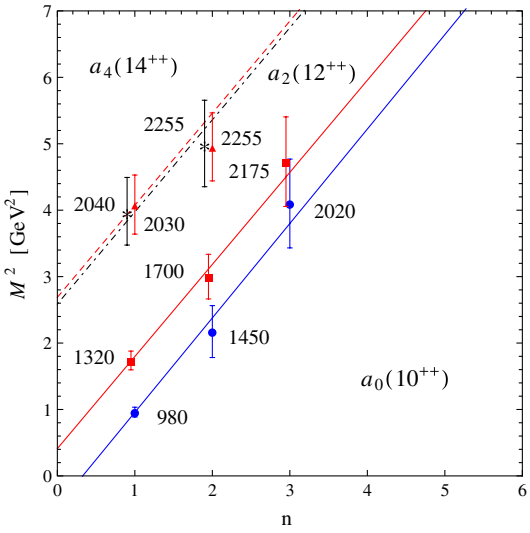

FIG. 6 (color online). The (n, M^2) plots for the $a_0(10^{++})$ (lower solid line), $a_2(12^{++})$ $q\bar{q}$ and $s\bar{s}$ (upper solid and dashed lines, respectively), and $a_4(14^{++})$ (dash-dotted line) trajectories. Error bars correspond to taking $\Delta M^2 = \pm\Gamma M$.

(i) The f_2^a trajectory (lower solid line in Fig. 7). It contains $f_2(1270)$, $f_2(1750)$, and $f_2(2150)$, one less state than Ref. [3] which also included $f_2(2400)$. In our case, the slope for this trajectory is $\mu^2 = 1.50(19)$ GeV^2 with $\chi^2/\mathrm{DOF} = 0.06$.

(ii) The f_2^b trajectory (dashed line in Fig. 7). It contains $f_2(1430)$, which is still to be determined (we take $M = 1468(60)$ MeV and $\Gamma = 100(100)$ MeV), $f_2(1910)$ with $M = 1927(32)$ MeV and $\Gamma = 154(73)$ MeV, and, finally, $f_2(2240)$. These states yield $\mu^2 = 1.48(23)$ GeV^2 with $\chi^2/\mathrm{DOF} = 0.09$.

(iii) The f_2^c trajectory (the upper solid line in Fig. 7.) As in Ref. [3], it is composed of $f_2(1525)$, $f_2(1950)$, and $f_2(2295)$, giving $\mu^2 = 1.47(25)$ GeV^2 with $\chi^2/\mathrm{DOF} = 0.000\,01$.

(iv) The f_2^d trajectory (the dash-dotted line in Fig. 7). It contains $f_2(1565)$ (which needs confirmation), $f_2(2000)$, and $f_2(2300)$. The slope for this trajectory is $\mu^2 = 1.42(20)$ GeV^2 with $\chi^2/\mathrm{DOF} = 0.05$. The states considered here involve some reshuffling compared to Ref. [3].

We now turn to the new trajectories, i.e., not given in Ref. [3], which are separately plotted in Fig. 7 (right panel).

(i) The two trajectories including $f_2(1640)$ and $f_2(2150)$ as well as $f_2(1810)$ and $f_2(2220)$ (both of them need confirmation), might actually be intertwined or describe an overcomplete set of states. The first one returns $\mu^2 = 1.99(36)$ GeV^2 and the second $\mu^2 = 1.69(36)$ GeV^2. Considering the lack of confirmation and the particular values for both masses and widths, it might turn out that $f_2(1810)$ and $f_2(2220)$ are the very same $f_2(1910)$ and $f_2(2240)$ states.

(ii) The upper trajectory is described with $\mu^2 = 1.43(83)$ GeV^2 and contains two states, $f_2(2010)$ and $f_2(2340)$.

G. $f_0(00^{++})$

Two trajectories for $f_0(00^{++})$ are displayed in Fig. 8 and as claimed in Ref. [3] they are doubled due to two flavor components, $q\bar{q}$ and $s\bar{s}$. Without considering the $f_0(600)$ (see however Ref. [36] and the Appendix), also called the σ meson, the lower trajectory contains four states: $f_0(980)$, $f_0(1500)$, $f_0(2020)$, and $f_0(2200)$ (solid line in Fig. 8). The last state was actually predicted in Ref. [3] and later confirmed experimentally. The trajectory yields $\mu^2 = 1.31(12)$ GeV^2 with $\chi^2/\mathrm{DOF} = 0.11$.

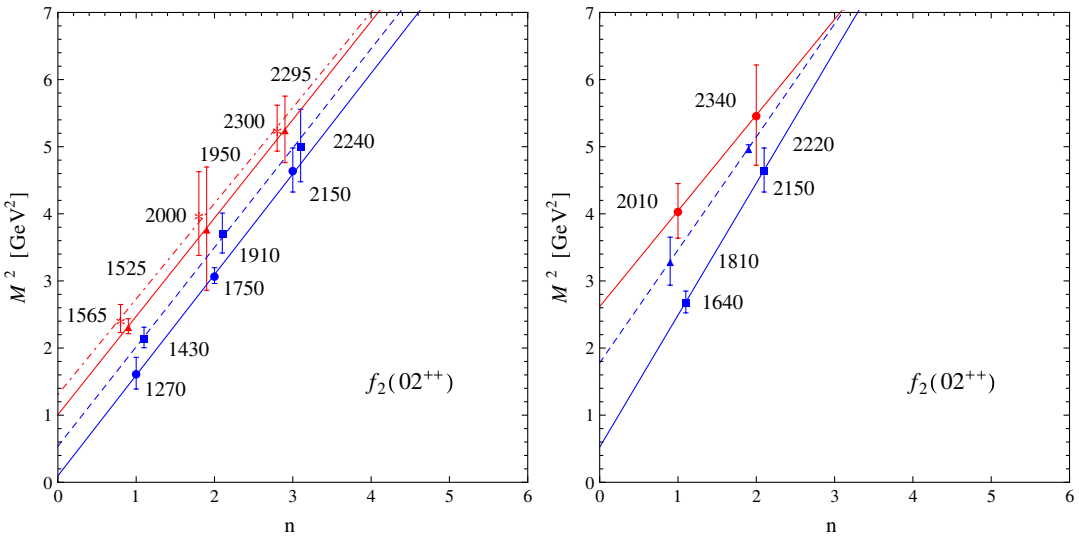

FIG. 7 (color online). The (n, M^2) plots for the seven $f_2(02^{++})$ trajectories comprising the 4 originally described in Ref. [3] (left panel) and the new ones discussed in the main text (right panel). Error bars correspond to taking $\Delta M^2 = \pm\Gamma M$.

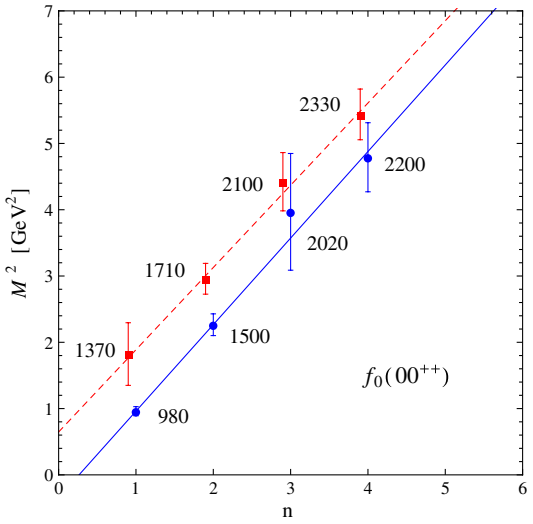

FIG. 8 (color online). The (n, M^2) plot for the $f_0(00^{++})$ $q\bar{q}$ (solid line) and $s\bar{s}$ (dashed line) trajectories. Error bars correspond to taking $\Delta M^2 = \pm\Gamma M$.

The second trajectory (dashed line in Fig. 8) has also four states, $f_0(1370)$, $f_0(1710)$, $f_0(2100)$, and $f_0(2330)$, where an average of the experimental determinations is considered for this latter state. It yields $\mu^2 = 1.24(18)$ GeV^2 with $\chi^2/\mathrm{DOF} = 0.12$.

H. $\omega(01^{--})$ and $\omega_3(03^{--})$

After reanalyzing the radial Regge trajectories taken into account in Ref. [3], we now analyze using the same methodology the remaining meson families included in the latest PDG review [4].

Two trajectories for the $\omega(01^{--})$ states are shown in Fig. 9. The ordering of the states on the different trajectories for the ω-family follows very closely the classification of the ρ-family states, Fig. 4. The main ω-trajectory, representing the $q\bar{q}$ states and drawn as a solid line in Fig. 9, contains four states: $\omega(782)$, $\omega(1420)$, $\omega(1960)$, and $\omega(2205)$. The slope from the fit is $\mu^2 = 1.50(12)$ GeV^2 with $\chi^2/\mathrm{DOF} = 0.32$.

The daughter trajectory (dashed line in Fig. 9) contains two states: $\omega(1650)$ and $\omega(2290)$. In the PDG recollection, two ω states with very similar masses are listed in the 2.3 GeV region: $\omega(2290)$ and $\omega(2330)$. Looking at the error determination of the parameters of these states, it is not clear to us that the two states are indeed different. We gather both experimental results in a single entry $\omega(2290)$, which has mass 2315(45) MeV and width 325(185) MeV. Comparing this trajectory with the corresponding one from the ρ-family, we notice a missing ω state with the mass near 2000 MeV, indicating the state $\omega(2290)$ to be the third on its trajectory. With only two states, the corresponding slope is $\mu^2 = 1.27(47)$ GeV^2.

The third trajectory in Fig. 9, describing the $\omega_3(03^{--})$ states, contains $\omega_3(1670)$, $\omega_3(1945)$, and $\omega_3(2255)$. It yields $\mu^2 = 1.16(26)$ GeV^2 with $\chi^2/\mathrm{DOF} = 0.37$.

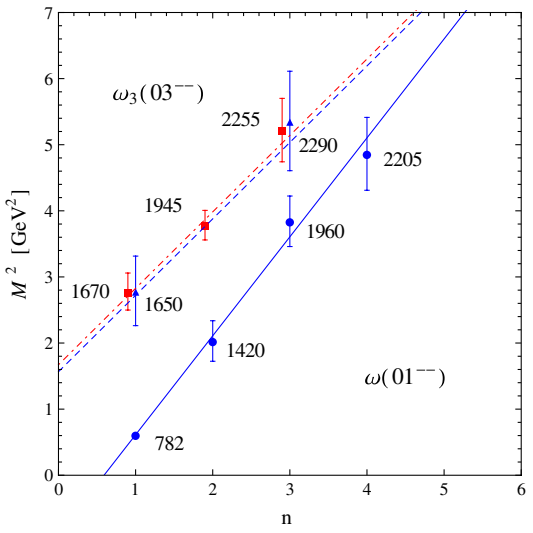

FIG. 9 (color online). The (n, M^2) plot for the $\omega(01^{--})$ (circles, solid line and triangles, dashed line) trajectories, as well as for the $\omega_3(03^{--})$ (squares,dash-dotted line) trajectory. Error bars correspond to taking $\Delta M^2 = \pm\Gamma M$.

I. $h_1(01^{+-})$ and $h_3(03^{+-})$

The h sector contains two trajectories corresponding to the $h_1(01^{+-})$ and $h_3(03^{+-})$ states shown as circles and squares in Fig. 10, respectively. The $h_1(01^{+-})$ case consists of four states: $h_1(1170)$, $h_1(1595)$, $h_1(1965)$, and $h_1(2215)$. The $h_1(1380)$ state is excluded, since it still needs to be confirmed. The linear fit to this trajectory, shown as a solid line in Fig. 10, gives $\mu^2 = 1.20(25)$ GeV^2 with $\chi^2/\mathrm{DOF} = 0.01$.

The $h_3(03^{+-})$ includes only two states, $h_3(2025)$ and $h_3(2275)$ (supposed to be the second and third excitation

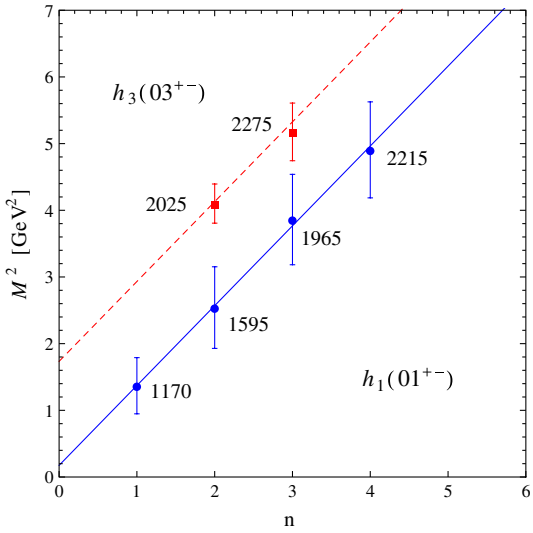

FIG. 10 (color online). The (n, M^2) plot for the $h_1(01^{+-})$ (circles, solid line) and $h_3(03^{+-})$ (squares, dashed line) trajectories. Error bars correspond to taking $\Delta M^2 = \pm\Gamma M$.

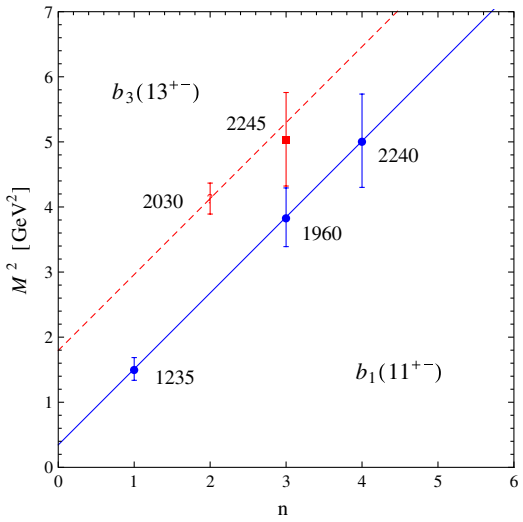

FIG. 11 (color online). The (n, M^2) plot for the $b_1(11^{+-})$ (circles, solid line) and $b_3(13^{+-})$ (squares, dashed line) trajectories. Error bars correspond to taking $\Delta M^2 = \pm\Gamma M$.

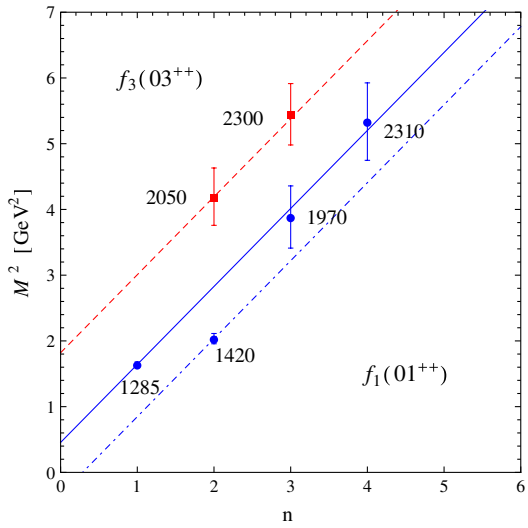

FIG. 12 (color online). The (n, M^2) plot for the $f_1(01^{++})$ (circles, solid line) and $f_3(03^{++})$ (squares, dashed line) trajectories. Error bars correspond to taking $\Delta M^2 = \pm\Gamma M$.

states of that trajectory), thus the slope $\mu^2 = 1.08(54)$ GeV^2 is determined. In Fig. 10, the dashed line, drawn parallel to the solid line, represents this trajectory.

J. $b_1(01^{+-})$ and $b_3(03^{+-})$

Similarly to the previous subsection, the b sector contains two trajectories, corresponding to the $b_1(11^{+-})$ and $b_3(13^{+-})$ states, shown as circles and squares in Fig. 11, respectively. The $b_1(01^{+-})$ consists of three states: $b_1(1235)$, $b_1(1960)$, and $b_1(2240)$. The linear fit returns $\mu^2 = 1.17(18)$ GeV^2 with $\chi^2/\mathrm{DOF} = 0.000\,01$ (solid line in Fig. 11).

The $b_3(03^{+-})$ includes only two states, $b_3(2030)$ and $b_3(2245)$, hence the slope is $\mu^2 = 0.93(75)$ GeV^2. In Fig. 11, a dashed line, parallel to the solid line, represents this trajectory. Since the resemblance between the h sector and the b sector is apparent, that suggests the existence of a still not determined b_1 state with a mass of the order of 1600 MeV.

K. $f_1(01^{++})$ and $f_3(03^{++})$

The situation with the f_1 and f_3 states is equivalent to the b and h case, thus we have two different trajectories corresponding to the different angular-momentum, $f_1(01^{++})$ and $f_3(03^{++})$, shown as circles and squares in Fig. 12, respectively. The $f_1(01^{++})$ trajectory consists of three states: $f_1(1285)$, $f_1(1960)$, and $f_1(2240)$. The fit for this trajectory returns $\mu^2 = 1.19(15)$ GeV^2 with $\chi^2/\mathrm{DOF} = 0.13$ and it is shown as a solid line in Fig. 12.

The $f_3(03^{++})$ includes only two states, $f_3(2050)$ and $f_3(2300)$. The slope is $\mu^2 = 1.27(64)$ GeV^2. In Fig. 12, the dashed line, drawn parallel to the solid line, displays this trajectory. The location of these states follows closely the case of $h_3(03^{+-})$ and $b_3(13^{+-})$, hence it starts at the radial quantum number $n = 2$. From Fig. 12, it is not obvious how to allocate the $f_1(1420)$ state, since the departure from the expected value seems much larger than expected from the half-width rule, therefore we exclude it from the fit. This choice resembles the h_1 case.

L. $\phi(01^{--})$ and $\phi_3(03^{--})$

The ϕ sector has three states with $J = 1$ ($\phi(1020)$, $\phi(1680)$, and $\phi(2170)$), and one with $J = 3$ ($\phi_3(1850)$), therefore the allocation of states becomes less unique. However, if the states with $J = 1$ are placed on a radial linear trajectory, a well-determined slope $\mu^2 = 1.84(6)$ GeV^2 with a $\chi^2 = 0.06$ is obtained. We note that such slope is much larger than any of the other slopes found so far. We could also concede the states $\phi(1680)$, and $\phi(2170)$ to be $n = 2, 3$, respectively, which would produce $\mu^2 = 1.19(4)$ GeV^2 instead, although with too large $\chi^2/\mathrm{DOF} = 6.4$. Because of this ambiguity, we will not consider this family for the final summary results

In Fig. 13, two trajectories are shown as parallel lines, with a solid line representing the $J = 1$ states, and the dashed line going across the $J = 3$ state. Clearly, this somewhat disturbing picture should profit from both theoretical or experimental insight.

M. $\pi_1(11^{-+})$

Finally, the last sector we analyze corresponds to the π_1 states, composed by $\pi_1(1400)$, $\pi_1(1600)$, and $\pi_1(2015)$. Two different measurements are found for this last state and we average them to have mass $M = 2.013(25)$ GeV and width $\Gamma = 0.287(53)$ GeV.

With these three states on a linear trajectory, the slope obtained is $\mu^2 = 1.09(36)$ GeV^2 with a $\chi^2 = 0.11$. The results are depicted in Fig. 14.

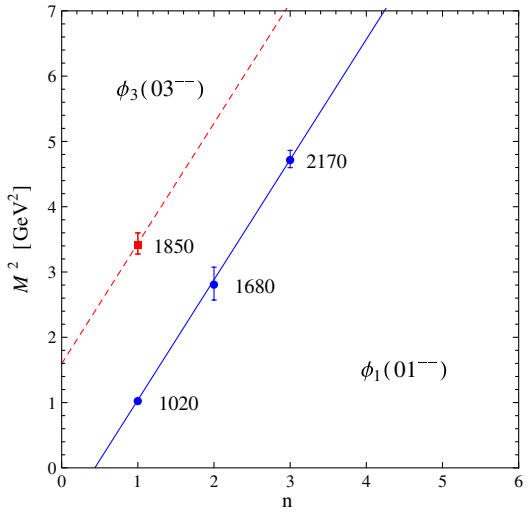

FIG. 13 (color online). The (n, M^2) plot for the $\phi(01^{--})$ (circles, solid line) and $\phi_3(03^{--})$ (squares, dashed line) trajectories. Error bars correspond to taking $\Delta M^2 = \pm\Gamma M$.

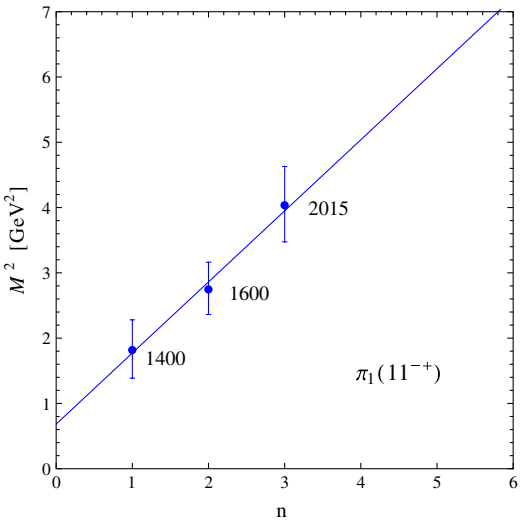

FIG. 14 (color online). The (n, M^2) plot for the $\pi_1(11^{-+})$ (circles, solid line) trajectories. Error bars correspond to taking $\Delta M^2 = \pm\Gamma M$.

N. Summary of the radial-trajectory fits

We summarize this section by collecting the fits for all the radial trajectories studied. The μ^2 parameter ranges from 1.09(36) GeV^2 (the $\pi_1(11^{-+})$ trajectory) to 1.50(19) GeV^2 (corresponding to the $f_2^a(02^{++})$ trajectory). The weighted average yields [6]

$$\mu^2 = 1.35(4)\ \text{GeV}^2. \tag{5}$$

This result agrees within the uncertainties with the estimate of Ref. [3], $\mu^2 = 1.25(15)$ GeV^2, where the uncertainty was given by the spread of the mean values determined from a fit to the PDG masses with equal weights. When we carry out the same procedure for the updated and *new* trajectories, we get $\mu^2 = 1.32(12)$ GeV^2. This seems to provide a quite robust estimate of a *common* radial Regge trajectories slopes. A graphic overview of the estimated slopes is presented in Fig. 16 (upper part).

We have also considered the possibility of a linear n-dependence of the masses, since it was a popular outcome of holographic models in the hard-wall scheme (see, e.g., Ref. [28] and references therein). With the same conditions as analyzed above, i.e., assuming the validity of the half-width rule our analysis is not compatible with such radial spectrum; typically, we obtain $\chi^2/\text{DOF} \sim 10$ or larger.

IV. (J, M^2) TRAJECTORIES

In this section, taking into account all the states so far considered and adding those with larger $J = 4, 5, 6$ from the PDG tables [4], we complement the results of the (n, M^2) analysis with the study in the (J, M^2) plane, i.e, the standard Chew-Frautschi plots [5].

One may parametrize the trajectories as

$$\alpha_X(M^2) \sim \alpha_X(0) + \alpha'_X(0)M^2, \tag{6}$$

with $\alpha_X(0)$ and $\alpha'_X(0)$ constant parameters.

Equivalently, we consider

$$M_X^2(J) = M_X^2(0) + \beta_X J. \tag{7}$$

The β parameter is related to α as $\beta \sim 1/\alpha'_X(0)$.

The results for the leading trajectories are shown in Table I. Generally, we do not attempt to determine the slope when the trajectory is made of less than three states. An overview of the estimated slopes can be seen in Fig. 16 (lower part). Nevertheless, to provide a broader perspective, we show in Fig. 15 also trajectories with just two states (dashed lines).

The weighted average result for the angular trajectories yields

$$\beta = 1.16(4)\ \text{GeV}^2. \tag{8}$$

If one considers, instead, the spread of central values as in Ref. [3], the updated result for the states, one obtains $\beta = 1.15(8)$ GeV^2, in agreement with [3].

When comparing the results of Eqs. (5) and (8), we note that the radial and angular-momentum slopes are different at the level of 3.4 standard deviations. Thus, there is indication that the *radial slopes are larger than the angular-momentum slopes* at a significant statistical level. We come back to this important issue in the next section.

It should be noted that in addition to the states of Ref. [3], we have also included the ω, h_1, b_1, f_1, ϕ, and

[6] We use the customary definition for the weighted average $\bar{A} = \sum_{i=1}^N w_i A_i / \sum_{i=1}^N w_i$, with $w_i = 1/\sigma_i^2$. The errors are the mean-squared deviation, $\sqrt{\bar{A}^2 - (\bar{A})2}$. The mean average corresponds to $w_i = 1$.

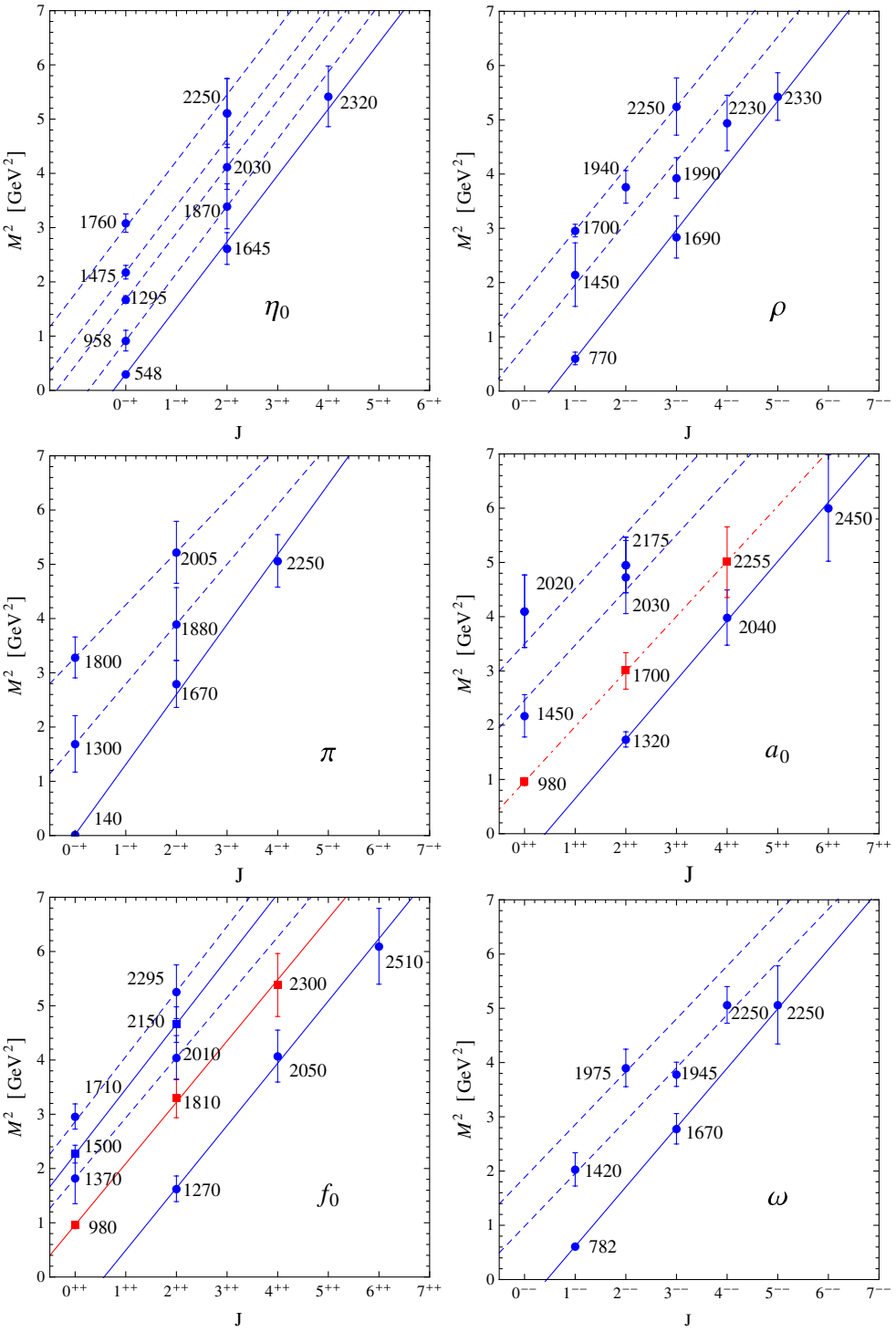

FIG. 15 (color online). The (J, M^2) plots for all states considered in Table I. Error bars correspond to taking $\Delta M^2 = \pm\Gamma M$.

π_1 sectors on our analysis, as well as three new J-trajectories, with the a_0, f_0, and ω states.

V. JOINT (n, J, M^2) FITS

A summary of the estimated radial and angular slopes is given in Fig. 16. We consider a weighted average estimate for a common (universal) slope trajectory, including the studied trajectories both in the (n, M^2) and the (J, M^2) planes. This yields $\mu^2 = \beta = 1.26(3)$ GeV^2. When the spread of central values for all the trajectories is used, we obtain $\mu^2 = \beta = 1.27(14)$ GeV^2. The trend to produce a number closer to the radial slope reflects a larger sample. As a matter of fact, when we weight both n and J trajectories equally, we get $\mu^2 = \beta = 1.26(3)$ GeV^2.

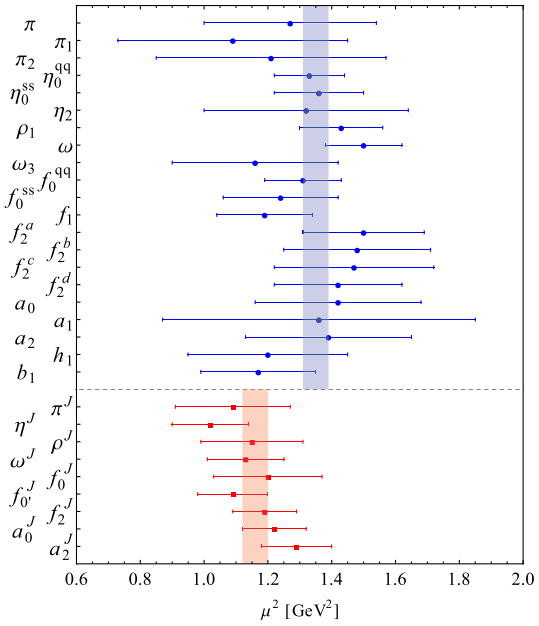

FIG. 16 (color online). (n, M^2) and (J, M^2) slope results for the considered trajectories. The horizontal dashed line separates the radial slopes (circles) from the angular slopes (squares). Individual errors are estimated from the χ^2 fits to the corresponding trajectories described in the main text. The bands correspond to the weighted averages of the radial (upper band) and the angular-momentum (lower band).

In the previous sections, we have carried out the analysis for the (n, M^2) and (J, M^2) planes, with the indication that $\mu^2 > \beta$ at a significant statistical level (3.4 standard deviations). This strongly suggests a careful reconsideration of the findings of Ref. [15], where a common fit of Eq. (3) for the (n, M^2) and (J, M^2) planes was proposed. Technically, the joint analysis presented in this section is different from

TABLE I. The (J, M^2) trajectories for leading and daughter trajectories. For an easy comparison with Ref. [3], we also show the corresponding $\alpha'_X(0) \sim 1/\beta$ for each trajectory.

X	$M_X^2(0)$ [GeV^2]	β_X [GeV^2]	$\alpha'_X(0)$ [GeV^{-2}]	χ^2/DOF
η	0.30(0)	1.22(10)	0.82(7)	0.37
ρ	0.60(11)	1.19(10)	0.84(7)	0.15
π	0.018(0)	1.29(11)	0.78(7)	0.26
a_2	−0.45(43)	1.09(18)	0.92(15)	0.03
a_0	0.96(7)	1.02(12)	0.98(12)	0.001
f_2	−0.66(48)	1.15(16)	0.87(12)	0.12
f_0	2.26(16)	1.20(17)	0.83(12)	0.01
f'_0	0.96(7)	1.13(12)	0.88(9)	0.07
ω	−0.48(11)	1.09(11)	0.92(9)	0.02

the separate analyses of Secs. III and IV in the following important detail. In the separate fits, the constants M_0^2 and $M_0'^2$ in the formulas $M^2(n) = \mu^2 n + M_0^2$ and $M^2(n) = \beta J + M_0'^2$ were treated as unrelated parameters, even in the same family of states. On the contrary, formula (3), with a common parameter c for a given family, relates the "offset" constants M_0^2 and $M_0'^2$, providing a constraint to the statistical analysis.

Therefore, to look closer at the issue of universality of the radial and angular-momentum slopes, we analyze each sector independently with two different plane fit functions: the nonuniversal formula

$$M^2 = an + bJ + c \tag{9}$$

on one hand, and the universal formula

$$M^2 = a(n + J) + c \tag{10}$$

on the other hand. With the c parameter fixed for the whole family, the states with different values of n and J belong to

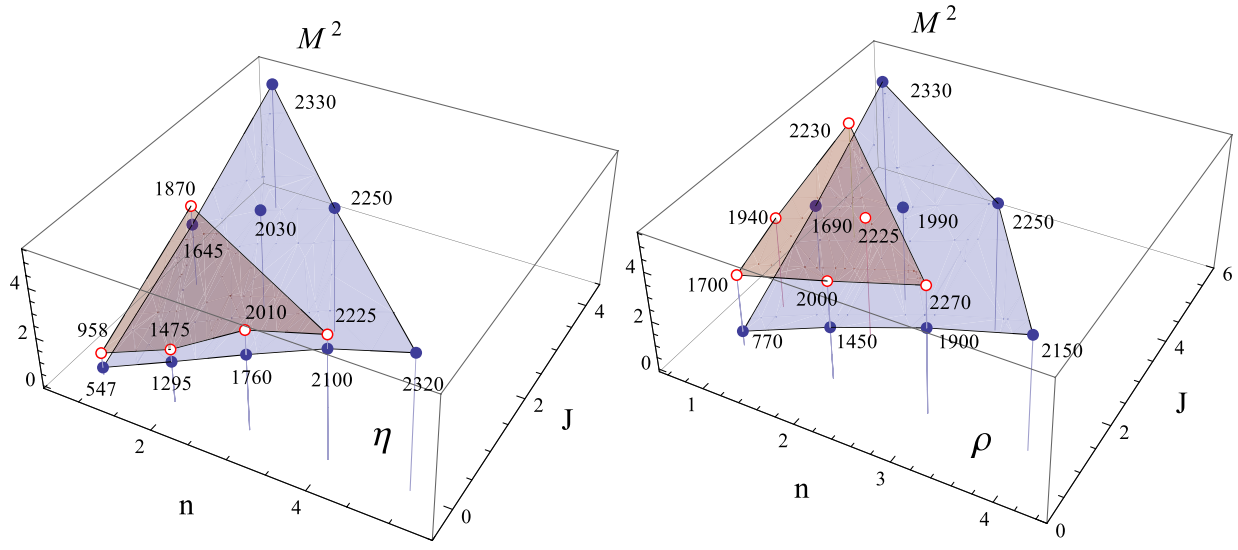

FIG. 17 (color online). The (n, J, M^2) Regge planes for the η family and the ρ family.

TABLE II. Regge-plane fits combining both radial and angular-momentum trajectories (see main text for details).

	$M^2 = an + bJ + c$				$M^2 = a(n + J) + c$		
	a	b	c	χ^2/DOF	a	c	χ^2/DOF
a_{13}	1.41(45)	1.11(32)	−1(1)	0.09	1.20(28)	−0.89(94)	0.19
η_{024}	1.36(5)	1.21(9)	−1.06(5)	0.22	1.33(4)	−1.03(4)	0.51
$\eta_{02_{ss}}$	1.36(14)	1.27(22)	−0.50(28)	0.44	1.34(13)	−0.47(27)	0.35
ρ_{135}	1.36(12)	1.12(9)	−1.87(23)	0.40	1.21(7)	−1.79(22)	0.73
π_{024}	1.47(10)	1.27(10)	−1.45(10)	0.29	1.36(6)	−1.34(6)	0.50
a_{246}	1.35(25)	1.06(16)	−1.75(48)	0.14	1.15(13)	−1.70(48)	0.33
a_{02}	1.35(24)	0.78(24)	−0.39(27)	0.53	1.06(9)	−0.09(13)	0.90
f_{0246}	1.38(13)	0.64(8)	0.04(33)	0.85	0.76(8)	1.06(29)	5.03
f_{02}	1.34(11)	0.69(6)	−0.38(15)	0.14	0.84(6)	0.13(11)	5.66
ω_{135}	1.42(11)	0.98(8)	−1.78(11)	0.63	1.16(5)	−1.70(10)	1.77
h_{13}	1.17(23)	0.75(19)	−0.53(62)	0.02	0.93(13)	−0.37(61)	0.46
b_{13}	1.15(17)	0.72(15)	−0.35(32)	0.05	0.91(9)	−0.29(32)	0.88
f_{13}	1.19(15)	0.70(19)	−0.24(17)	0.07	0.98(8)	−0.33(17)	0.95
ϕ_{13}	1.84(6)	1.20(08)	−2.0(1)	0.06	1.59(5)	−2.15(10)	19.5

a *Regge plane*. This is illustrated in Fig. 17 for the ρ- and η-families as an example.

Our numerical results are collected in Table II. Several meson sectors can be placed on two almost parallel planes. The nomenclature used is as follows: after the name of each family, the subindex quoted refers to the states with the particular angular quantum number used on the plane. For example, ρ_{135} means the set of all the ρ states with angular-momentum $J = 1, 3, 5$, and with all the possible radial quantum numbers.

The numbers in Table II show a few interesting features. The most important one is that for each family of states the fit with Eq. (9) is preferred over the fit with Eq. (10) (judging by the different χ^2/DOF values). Moreover, we generically find $a > b$. The offset parameter c also seems to be stable through all the planes, although less stable than the radial and angular slope parameters.

The fact that the ratio of the radial to angular slope, denoted as R, grows with the quark mass may be a generic and physically relevant feature. Note that for the heavy quarkonia the joint fit is compatible with the formula $M^2 = a(2n + J) + c$ [40]. Thus, it may be that R is close to unity for light mesons, $R = 2$ for heavy mesons, and assumes an intermediate value for hidden-strangeness states.

From Table II, it is worth stressing how close the states from the ρ and the ω families are. For a_{02} plane, we have assigned to $a_2(2030)$ and $a_2(2255)$ radial quantum numbers $n = 2$ and 3, respectively. Otherwise (with $n = 1$ and 2), the angular slope would be larger than the radial slope. The h_{13}, b_{13}, and f_{13} have systematically smaller a and b parameters from the remaining families, although very similar among themselves. As commented already, this fact may be caused by the lack of states in these sectors. States with higher angular-momentum (when discovered) would lead to better and more reliable determination of the Regge-plane parameters. Similar comments apply to the ϕ_{13} plane.

Considering only the planes with no large hidden-strangeness content and with six or more states (excluding then the h_{13}, b_{13}, f_{13}, and ϕ_{13} planes),[7] we obtain our global fit with the result

$$M^2 = 1.38(4)n + 1.12(4)J - 1.25(4). \quad (11)$$

Therefore, the $a = \mu^2$ parameter reads $a = 1.38(4)$ GeV^2 for the global Regge-plane fit, compatible with Eq. (5). The $b = \beta$ parameter reads $b = 1.12(4)$ GeV^2, also close to the value of Eq. (8). We note that $a > b$ at the level of 4.5 standard deviations. In this estimate, we take the geometric average of the individual errors (equal 0.04) for the standard deviation of the difference $a - b$. Therefore, the joint analysis points at a lack of universality of the Regge slopes.

The right part of Table II shows the result of the fit, where universality is imposed. This fit cannot be statistically rejected based on the values of χ^2, however, it is somewhat worse than without the universality constraint.

VI. CONCLUSIONS

In this paper, we have reanalyzed, with the help of the up-to-date PDG tables [4], the linear radial and angular-momentum Regge trajectories considered in Ref. [3], including in the fits the width of each state as an estimate of the error of the resonance mass (the half-width rule). As we have explained, this is a reasonable way to smooth out resonance profile information, which makes the very defi-

[7]The f_{02} is not considered either due to the arbitrariness on the selection of its components.

nition of the resonance mass ambiguous. Moreover, this choice allows to undertake an error analysis, not carried out in Ref. [3]. Furthermore, we have argued that such a procedure fully complies to the large-N_c viewpoint and actually suggests an interesting interpretation: the Regge-fitted masses are considered to be the leading-N_c contribution to the mass of the resonance. This incorporates a desirable flexibility as to what should the Regge fit be compared to. The squared mass of each meson is then represented as $M_n^2 = M^2 \pm \Gamma M$, where M is its mass and Γ is its width.

Generally, we reproduce the results of Ref. [3] when no uncertainties are included. This only reflects the robustness of the main features of the PDG compilation along the last 10 years, although some numerical values of the masses have changed and, furthermore, some new states, partly predicted by the pioneering radial Regge analysis of Ref. [3], have been added. From our results, it follows that there is no need to consider further new states to get an acceptable Regge description. This is consistent with an assertion of a complete mesonic spectrum up to the highest energies considered in our work.

We have also addressed the issue of the *universality* of radial and angular-momentum slopes within the errors deduced from the linear-regression analysis with weights provided with the half-width rule. Our joint analysis in the (n, J, M^2) Regge planes indicates, at a statistically significant level of 4.5 standard deviations, that the radial slope is larger from the angular-momentum slope. Thus, no strict universality of slopes occurs in the light nonstrange meson spectra.

ACKNOWLEDGMENTS

Supported by MICINN of Spain (FPA2010-16802, FPA2010-16696, FIS2011-24149) and Consolider-Ingenio 2010 Programme CPAN (CSD2007-00042), by Junta de Andalucía (FQM 101, FQM 437, FQM225, and FQM022) and by the Polish Science and Higher Education, Grant No. N N202 263438, and National Science Centre, Grant No. DEC-2011/01/D/ST2/00772.

APPENDIX: DEPENDENCE ON RESONANCE PROFILE

In this Appendix, we show the independence of our results on the shape of the resonance profiles, and hence support our χ^2-statistical treatment. The χ^2-nature of the fit relies implicitly on the assumption that the probability of having a resonance with mass M and width Γ is of a Gaussian shape,

$$P(\sqrt{s}) = Ce^{-((\sqrt{s}-M)^2/\Gamma M)}, \tag{A1}$$

with C a normalization constant, whereas for the squared mass one has

$$P(s) = C'e^{-((s-M^2)^2/2\Gamma^2 M^2)}. \tag{A2}$$

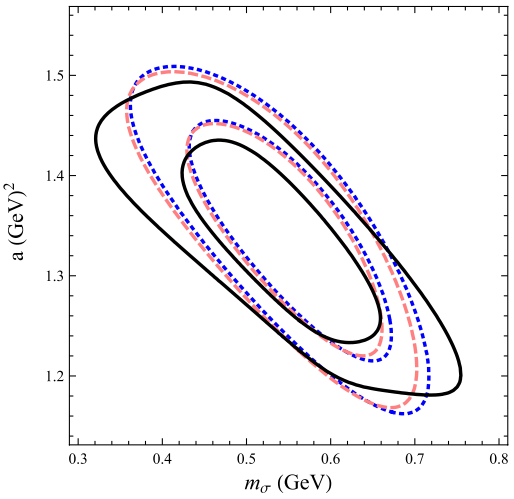

FIG. 18 (color online). The 68% and 95% relative confidence-level contours of the radial Regge trajectories for all scalars in the PDG assuming several resonance profiles. (1) Gaussian at the level of the mass (dashed line), (2) Gaussian at the level of the squared mass (dotted line), and (3) Breit-Wigner shape (black solid line).

The χ^2-fit then corresponds to applying the maximum-likelihood method and maximize with respect to a and M_0 the function

$$L(a, M_0; \{\Gamma_n, M_n\}) = \prod_{n=1}^{N} P(s_n, \Gamma_n, M_n), \tag{A3}$$

where $s_n = an + M_0^2$. This is the way the half-width rule is implemented in practice, i.e., by assuming short tails in the mass distribution. On the other hand, from analyticity arguments the resonance profile function should be of a Breit-Wigner (BW) form, at least for sufficiently narrow resonances. Let us consider for definiteness the parametrization of a complex resonance propagator at a given CM energy squared, s,

$$D(s) = \frac{1}{s - M^2 - i\Gamma\sqrt{s}}. \tag{A4}$$

The $\sqrt{s}$ in the denominator ensures that we have a pole on the second Riemann sheet (we neglect threshold effects). Likewise, we also have a pure imaginary amplitude at the real resonance value $s = M^2$. The probability for such a mass distribution corresponds to the imaginary part,[8] namely,

$$P_{\mathrm{BW}}(s) = Z\frac{\Gamma\sqrt{s}}{(s - M^2)^2 + \Gamma^2 s}, \tag{A5}$$

[8]We are appealing to the Lehman representation for a resonance as obtained from a CM-energy dispersion relation of the scattering process, see, e.g., Ref. [41] for a discussion in the context of the $\pi\pi$-scattering.

where Z is a suitable normalization constant. Thus, we may apply the maximum-likelihood method to Eq. (A3) for N resonances fulfilling the Regge formula and maximize with respect to a and M_0.

As a specific example, to illustrate the difference between the Gaussian, Eq. (A2), and the Breit-Wigner, Eq. (A5), profiles to the set of all 0^{++} scalars listed in the PDG (see also Fig. 8) as discussed in Refs. [34,36], where a joint formula for the trajectories,

$$s_n = \frac{a}{2} n + m_\sigma^2, \tag{A6}$$

was proposed. Maximizing $P(a, m_\sigma; \{M_n, \Gamma_n\})$ with respect to a and m_σ and using Eqs. (A1), (A2), and (A5), yields the most likely values $m_\sigma = 0.545$, 0.557, 0.562 GeV, and $a = 1.330$, 1.336, 1.334 GeV^2, respectively. The Gaussian cases correspond to the χ^2-analysis of Refs. [34,36]. Similarly to the χ^2-method, the errors can be determined by looking at the locus of the relative probability $P(a, m_\sigma)/P_{\max} \leq (e^{-\Delta\chi^2/2})$, which for two variables yields $\Delta\chi^2 = 2.3$ and 4.7 for the 68% and 95% confidence levels, respectively. We show the results in Fig. 18 where, as we can see, the resonance shape does not play a role.

Of course, one may object to the previous confidence-level analysis that for non-Gaussian probabilities mode (most likely) and mean (average) are different. Indeed, the application of

$$\langle A \rangle = \int da \int dm_\sigma A(a, m_\sigma) L_{\mathrm{BW}}(a, m_\sigma; \{M_n, \Gamma_n\}) \tag{A7}$$

yields $\langle a \rangle = 1.34$ GeV^2 and $\langle m_\sigma \rangle = 0.53$ GeV for the mean values, whereas the mode is at $m_\sigma = 0.562$ GeV and $a = 1.334$ GeV^2. Thus, for the Breit-Wigner case the mean and the mode are different and the errors are not defined by standard confidence-level rules with $\langle A \rangle \pm \sqrt{\langle A^2 \rangle - \langle A \rangle^2}$, for which we get $a = 1.34(8)$ GeV^2, $m_\sigma = 0.53(11)$ GeV with a correlation $r(a, m_\sigma) = -0.77$. A way to sort this out is to define the equal probability contours, to integrate inside the inner region for a given confidence level,

$$p(z) = \int da dm_\sigma P(a, m_\sigma) \Theta(P) a, m_\sigma(-z), \tag{A8}$$

and to search for a z such that $p(z) = 0.68$. The resulting contour resembles strongly Fig. 18, reinforcing the conclusion that the shape of the resonance profile is irrelevant for the analyses of this work.

[1] E. Klempt and A. Zaitsev, Phys. Rep. **454**, 1 (2007).
[2] M. Shifman, Czech. J. Phys. **52**, B102 (2002).
[3] A. V. Anisovich, V. V. Anisovich, and A. V. Sarantsev, Phys. Rev. D **62**, 051502 (2000).
[4] K. Nakamura *et al.* (Particle Data Group), J. Phys. G **37**, 075021 (2010).
[5] G. Chew and S. C. Frautschi, Phys. Rev. Lett. **7**, 394 (1961).
[6] P. Collins, Phys. Rep. **1**, 103 (1971).
[7] L. Susskind, Phys. Rev. D **1**, 1182 (1970).
[8] *Dual Theory*, edited by M. Jacob, Physics Reports reprint book series Vol. 1 (North-Holland, Amsterdam, 1974).
[9] P. Frampton, *Dual Resonance Models and Superstrings* (World Scientific, Singapore, 1986).
[10] D. Ebert, R. N. Faustov, and V. O. Galkin, Phys. Rev. D **79**, 114029 (2009).
[11] K. Huang and S. Weinberg, Phys. Rev. Lett. **25**, 895 (1970).
[12] R. Hagedorn, Nuovo Cimento Suppl. **3**, 147 (1965).
[13] W. Broniowski and W. Florkowski, Phys. Lett. B **490**, 223 (2000).
[14] W. Broniowski, W. Florkowski, and L. Y. Glozman, Phys. Rev. D **70**, 117503 (2004).
[15] S. Afonin, Phys. Lett. B **639**, 258 (2006).
[16] L. Glozman, Phys. Rep. **444**, 1 (2007).
[17] G. 't Hooft, Nucl. Phys. **B72**, 461 (1974).
[18] E. Witten, Nucl. Phys. **B160**, 57 (1979).
[19] A. Pich, arXiv:hep-ph/0205030.
[20] M. Harada, F. Sannino, and J. Schechter, Phys. Rev. D **69**, 034005 (2004).
[21] J. R. Pelaez, Phys. Rev. Lett. **92**, 102001 (2004).
[22] J. R. Pelaez and G. Rios, Phys. Rev. Lett. **97**, 242002 (2006).
[23] J. Nieves and E. Ruiz Arriola, Phys. Lett. B **679**, 449 (2009).
[24] J. Nieves and E. Ruiz Arriola, Phys. Rev. D **80**, 045023 (2009).
[25] J. Nieves, A. Pich, and E. Ruiz Arriola, Phys. Rev. D **84**, 096002 (2011).
[26] J. Nebreda, J. Pelaez, and G. Rios, Phys. Rev. D **84**, 074003 (2011).
[27] Z.-H. Guo and J. Oller, Phys. Rev. D **84**, 034005 (2011).
[28] J. Erdmenger, N. Evans, I. Kirsch, and E. Threlfall, Eur. Phys. J. A **35**, 81 (2008).
[29] A. Karch, E. Katz, D. T. Son, and M. A. Stephanov, Phys. Rev. D **74**, 015005 (2006).
[30] G. F. de Teramond and S. J. Brodsky, Phys. Rev. Lett. **102**, 081601 (2009).
[31] A. D. Martin and T. D. Spearman, *Elementary-Particle Theory* (North-Holland, Amsterdam, 1970).
[32] N. Suzuki, T. Sato, and T.-S. Lee, Phys. Rev. C **79**, 025205 (2009).
[33] R. Workman, R. Arndt, and M. Paris, Phys. Rev. C **79**, 038201 (2009).

[34] E. Ruiz Arriola and W. Broniowski, Bled Workshops in Physics **12**, 7 (2011).
[35] P. Masjuan and S. Peris, J. High Energy Phys. 05 (2007) 040.
[36] E. Ruiz Arriola and W. Broniowski, Phys. Rev. D **81**, 054009 (2010).
[37] S. Afonin, A. Andrianov, V. Andrianov, and D. Espriu, J. High Energy Phys. 04 (2004) 039.
[38] A. Tang and J. W. Norbury, Phys. Rev. D **62**, 016006 (2000).
[39] A. Anisovich, C. Baker, C. Batty, D. Bugg, V. Nikonov, A. Sarantsev, V. Sarantsev, and B. Zou, Phys. Lett. B **517**, 261 (2001).
[40] S. Gershtein, A. Likhoded, and A. a. Luchinsky, Phys. Rev. D **74**, 016002 (2006).
[41] A. Calle Cordon and E. Ruiz Arriola, Phys. Rev. C **80**, 014002 (2009).